

The warm absorber in the radio-loud quasar 4C +74.26

L. Di Gesu^{1,2} and E. Costantini¹

¹ SRON Netherlands Institute for Space Research, Sorbonnelaan 2, 3584 CA Utrecht, The Netherlands

² Department of Astronomy, University of Geneva, 16 Ch. d'Ecogia, 1290, Versoix, Switzerland e-mail: Laura.DiGesu@unige.ch

Received April 8, 2016; accepted June 13, 2016

ABSTRACT

Outflows of photoionized gas are commonly detected in the X-ray spectra of Seyfert 1 galaxies. However, the evidence for this phenomenon in broad line radio galaxies, which are analogous to Seyfert 1 galaxies in the radio-loud regime, has so far been scarce. Here, we present the analysis of the X-ray absorption in the radio-loud quasar 4C +74.26. With the aim of characterizing the kinetic and the ionization conditions of the absorbing material, we fitted jointly the XMM-Newton Reflection Grating Spectrometer (RGS) and the Chandra High Energy Transmission Grating Spectrometer (HETGS) spectra, which were taken 4 months apart. The intrinsic continuum flux did not vary significantly during this time lapse. The spectrum shows the absorption signatures (e.g., Fe-UTA, O VII, and Ne VII–Ne X) of a photoionized gas outflow ($N_{\text{H}} \sim 3.5 \times 10^{21} \text{ cm}^{-2}$, $\log \xi \sim 2.6$, $v_{\text{out}} \sim 3600 \text{ km s}^{-1}$) located at the redshift of source. We estimate that the gas is located outside the broad line region but within the boundaries of the putative torus. This ionized absorber is consistent with the X-ray counterpart of a polar scattering outflow reported in the optical band for this source. The kinetic luminosity carried by the outflow is insufficient to produce a significant feedback in this quasar. Finally, we show that the heavy soft X-ray absorption that was noticed in the past for this source arises mostly in the Galactic ISM.

Key words. galaxies: individual 4C +74.26 - quasars: absorption lines - quasars: general - X-rays: galaxies

1. Introduction

In the last fifteen years, thanks to the advent of high-resolution X-ray spectrometers, such as the XMM-Newton Reflection Grating Spectrometer (RGS) or the Chandra Low and High Energy Transmission Grating Spectrometers (LETGS and HETGS), our knowledge of the circumnuclear gaseous environment of active galactic nuclei (AGN) has advanced significantly. It is now established that roughly half of all local Seyfert galaxies host a photoionized warm absorber (WA) that produces features detectable in the X-ray and in the UV band (Crenshaw et al. 2003). These absorption lines are usually blueshifted with respect of the systemic velocity, which indicates a global outflow of the absorbing gas. Spectroscopical observations allow the physical conditions (kinematics and ionization) of the gas to be characterized with high accuracy (see Costantini 2010, for a review). In photoionization equilibrium, the ionization parameter $\xi = L_{\text{ion}}/nr^2$ (where L_{ion} is the ionizing luminosity between 1 and 1000 Ryd, n is the gas density, and r is the distance from the ionizing source) parameterizes the state of the gas. In the X-ray band, there are many transitions, for example from ionized C, N, O, Ne, and Fe, which allow an accurate solution for ξ to be determined. From spectroscopical observables, useful constraints can be put on the gas location (Blustin et al. 2005); these constraints quantify how much momentum is transferred by the outflow to the surrounding medium (e.g., Crenshaw & Kraemer 2012).

The studies of WA in Seyfert galaxies show that these outflows span roughly four orders of magnitude in ionization ($\log \xi \sim 0 - 4$) and reach velocities of a few thousand km s^{-1} (McKernan et al. 2007). They are often located as far as the putative torus (Blustin et al. 2005). Some outliers may be located closer to the nucleus, at the distance of the accretion disk or farther out in the galaxy at $\sim \text{kpc}$ distance from the center (Di

Gesu et al. 2013). In most of the cases, the kinetic power of the WA is found to be negligible with respect to the AGN radiative power (e.g., Ebrero et al. 2016). Thus, WA are not expected to play a significant role in a possible negative AGN feedback (Scannapieco & Oh 2004; Somerville et al. 2008; Hopkins et al. 2008; Hopkins & Elvis 2010; King & Pounds 2015).

A different class of photoionized winds are the ultrafast outflows (UFO). These may be present in 35% of Seyfert galaxies (Tombesi et al. 2010) and differ from classical WA because of the higher outflow velocity ($v \sim 0.1 c$, where c is the speed of light) and of the higher ionization ($\log \xi \geq 3$, Tombesi et al. 2011). Hence, because of the higher energy and higher blueshift of their transitions (e.g., Fe XXV–Fe XXVI), UFO are detectable only in lower resolution CCD spectra. These powerful winds are believed to be a nuclear phenomenon originating from the accretion disk (Tombesi et al. 2012; Nardini et al. 2015).

The detection of photoionized features in broad line radio galaxies (BLRG), which are analogous to Seyfert 1 galaxies in the radio-loud regime, was expected to be difficult because of the presence of a relativistic jet. The Doppler-boosted, non-thermal radiation of a jet located close to the line of sight could actually mask the absorption features. So far, the statistics of known WA in BLRG relies on a handful of cases, of which only three are WA detections in a high-resolution X-ray dataset. Hints of photoionized absorption were noticed, for instance, in the ROSAT-PSPC spectrum of 3C 351 (Fiore et al. 1993) and 3C 212 (Mathur 1994). Interestingly, these two sources also display WA features in the UV (Mathur et al. 1994; Yuan et al. 2002). More recently, Molina et al. (2015) have reported the detection of O VII and of Fe XX absorption edges in the EPIC-pn spectrum of IGR J14488-4008, a giant radio-loud galaxy discovered by INTEGRAL.

The first case of a WA in a BLRG studied with a grating spectrum was a long Chandra-HETGS spectrum of 3C 382

(Reeves et al. 2009). The detection of this WA, whose location is consistent with the distance of the narrow line region (NLR), was promptly confirmed by a subsequent RGS observation (Torresi et al. 2010). A second case is the remarkable photoionized outflow in 3C 445. In the *Chandra*-HETGS spectrum of this source Reeves et al. (2010) detected a low-ionization outflow moving at a sub-relativistic velocity. A deep Suzaku spectrum also shows indications of blueshifted absorption from highly ionized iron (Braitto et al. 2011). Both these spectra are consistent with a scenario where our line of sight intercepts an equatorial disk wind located at \sim sub-pc scale. The low-ionization absorber may consist of sparse clumps embedded in a highly ionized wind (Reeves et al. 2010). In addition to these two cases, Torresi et al. (2012) report a WA detection in the RGS spectrum of 3C 390.3.

Signatures of more highly ionized UFO have also been detected in the CCD spectra of a handful of radio-loud sources (Tombesi et al. 2014), with a statistical incidence comparable, within the uncertainties, to what is found for radio-quiet Seyferts.

In this paper we present the analysis of the X-ray grating spectrum – obtained with the RGS and the *Chandra* -HETGS – of the BLRG 4C +74.26. This source is located at a redshift of 0.104 (Riley et al. 1989). In the optical, it shows broad permitted lines with a $FWHM$ of $10\,000\text{ km s}^{-1}$ for the $H\beta$ line (Winter et al. 2010). Using this line width a SMBH mass of $3 \times 10^9 M_{\odot}$ is inferred.

Because of its ~ 1 Mpc projected linear size (Riley et al. 1989), this source is the largest known radio source associated with a quasar. Its radio morphology is typical for a Fanaroff-Riley type II source (FR II), although the 178 MHz radio luminosity is borderline with the type I class (FR I). Observations with the Very Large Array (VLA) have revealed a one-sided jet which is at least 4 kpc long (Riley & Warner 1990). The flux limit for a counter-jet, which could be set with a subsequent Very Long Baseline Interferometry (VLBI) observation (Pearson et al. 1992), implies that the source axis lies at $\lesssim 49^\circ$ from our line of sight.

Evidence of a high-velocity outflow in 4C +74.26 was found in the optical spectropolarimetric analysis performed in Robinson et al. (1999). These authors noticed that the broad $H\alpha$ line appears redshifted in polarized light, which can be explained if the scattering medium producing the polarization is part of a polar outflow.

Since 1993, 4C +74.26 has been targeted by many X-ray observatories, including ROSAT, ASCA, *Beppo*-SAX XMM-*Newton*, and *Suzaku*. In the XMM-*Newton* (Ballantyne & Fabian 2005) and in the *Suzaku* (Larsson et al. 2008) spectrum a broadened Fe $K\alpha$ emission line has been clearly detected at 6.4 keV. Recently, in the *Suzaku* (Gofford et al. 2013) and the XMM-*Newton* spectrum (Tombesi et al. 2014) additional absorption features in the Fe-K band have been noticed. These could be due to a highly ionized UFO, with a measured outflow velocity on the order of $\sim 0.1c$.

By studying the correlations between the *Suzaku* light curves in different bands, Noda et al. (2013) were able to extract the stable soft-excess component (Singh et al. 1985) that may dominate the continuum emission at soft energies (i.e., below 2.0 keV). According to these authors, the most likely origin for the soft-excess in this source is thermal Comptonization of the disk photons in a warm plasma (see, e.g., Noda et al. 2011; Done et al. 2012; Jin et al. 2012; Petrucci et al. 2013; Di Gesu et al. 2014; Giustini et al. 2015; Boissay et al. 2016).

It was found, however, that the soft-excess underlies a heavy soft

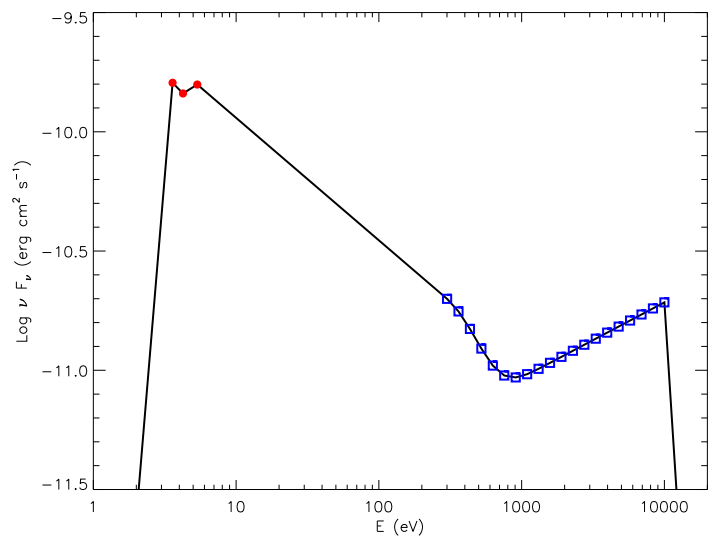


Fig. 1. Spectral energy distributions for 4C +74.26. Filled circles: OM fluxes corrected for the Galactic extinction. Open squares: X-ray intrinsic continuum obtained from a phenomenological fit of the EPIC-pn spectrum.

X-ray absorption. For instance, absorption from a substantial column density of gas in excess at the Galactic column density was seen earlier on in the ROSAT-PSPC (Brinkmann et al. 1998), ASCA (Brinkmann et al. 1998; Sambruna et al. 1999; Reeves & Turner 2000), and *Beppo*-SAX (Hasenkopf et al. 2002) spectra. In a more recent XMM-*Newton* observation, Ballantyne (2005) detected a column of cold absorption greater than the Galactic value, with an intrinsic column of $\sim 1.9 \times 10^{21}\text{ cm}^{-2}$. Moreover, the broadband XMM-*Newton* spectrum shows evidence of a weak WA intrinsic to the source. The WA is highlighted by features identified as the O VII and O VIII absorption edges (Ballantyne & Fabian 2005).

Motivated by these indications of a complex absorption in this source, here we use the archival XMM-*Newton* Reflection Grating Spectrometer (RGS) and *Chandra* High Energy Transmission Grating Spectrometer (HETGS) spectra of 4C +74.26 to characterize for the first time the kinematics and the ionization condition of the X-ray absorbing material.

In Sect. 2 we describe our data reduction procedure. Then in Sect. 3 we build the spectral energy distribution (SED), and in Sect. 4 we perform the spectral analysis. Finally, in Sect. 5 we discuss our results, and in Sect. 6 we state the conclusions.

The C-statistic (Cash 1979) is used throughout the paper, and errors are quoted at the 68% confidence level ($\Delta C = 1.0$). In all the spectral models presented, we use the total Galactic hydrogen column density from Willingale et al. (2013, $N_{\text{H}} = 2.31 \times 10^{21}\text{ cm}^{-2}$). In our luminosity calculations we use a cosmological redshift of $z=0.104$ and a flat cosmology with the following parameters: $H_0=70\text{ km s}^{-1}\text{ Mpc}^{-1}$, $\Omega_m=0.3$, and $\Omega_\Lambda=0.7$.

2. Observations and data preparation

The radio-loud galaxy 4C +74.26 was observed with *Chandra* and XMM-*Newton* in October 2003 and February 2004, respectively. Thus, the time separation between these X-ray observations is only 4 months. In Table 1 we summarize the basic information of each observation.

Chandra observed 4C +74.26 for ~ 70 ks in total using the HETGS in combination with the ACIS detector. The total exposure time was split into two observations that were taken

Table 1. XMM-Newton and *Chandra* observation log for 4C +74.26.

Date	Instrument	Observation ID	Net exposure ^a (ks)	$F_{0.3-2.0\text{keV}}^b$ (10^{-11} erg s ⁻¹ cm ⁻²)	$F_{2.0-10.0\text{keV}}^b$ (10^{-11} erg s ⁻¹ cm ⁻²)
2003 Oct 6	HETGS	4000	37	0.7	2.8
2003 Oct 8	HETGS	5195	31	0.8	2.9
2004 Feb 6	RGS	0200910201	34	0.9	3.0

Notes. ^(a) Resulting exposure time after correction for background flares. ^(b) Observed flux in the quoted bands.

two days apart. For both Obs-ID 4000 and 5195 we retrieved the Medium (MEG) and High Energy Grating (HEG) spectra and their respective response matrices from the *tgcat*¹ archive. We further treated these spectral products with the CIAO tools (version 4.6). For each observation and for both HEG and MEG, we combined the first positive and negative spectral order using the CIAO script `add_spectral_orders`. Hence, we fitted jointly HEG and MEG (allowing a free intercalibration factor) with a simple phenomenological power law to check for variability between the two observations. The fitted slopes ($\Gamma_{4000} = 1.32 \pm 0.02$, $\Gamma_{5195} = 1.34 \pm 0.02$) and normalizations ($Norm_{4000} = (9.9 \pm 0.1) \times 10^{53}$ ph s⁻¹ keV⁻¹, $Norm_{5195} = (10.5 \pm 0.2) \times 10^{53}$ ph s⁻¹ keV⁻¹) were very consistent with each other (see below for a physically motivated fit). Therefore, we were able to sum the spectra of individual observations into a single spectrum to improve the signal-to-noise ratio. We did this using the CIAO script `add_grating_spectra`.

We reduced the raw XMM-Newton Observation Data Files (ODF), available at the ESA archive², using the Science Analysis Software (SAS, version 13) and the HEASARC FTOOLS. We created calibrated EPIC-pn event files selecting only the unflagged single events. To check the time stability of the background we used the light curve in the hard 10–12 keV band, which is background dominated. A high level of background light due to soft proton contamination is evident towards the end of the observation. Thus, we cleaned the event file using a time filter, following the same procedure explained in Di Gesu et al. (2013). For RGS-1 and RGS-2 we created calibrated event files and background light curves taking the background from CCD 9. The RGS background light curve was quiescent. Next, for all the instruments, we extracted the source and background spectra and we created the spectral response matrices.

Finally, we extracted the source count rate in all the available OM filters, namely *U* ($\lambda_{\text{eff}} = 3440$ Å), *UVW2* ($\lambda_{\text{eff}} = 2910$ Å) and *UVM2* ($\lambda_{\text{eff}} = 2310$ Å). Using the interactive SAS tool `omsources`, we computed the source count in a circular region centered on the source coordinates and with a radius of 6 pixels. For the background we used another circular region of 12 pixels, free from other sources and instrumental contamination. We converted the count rates to fluxes using the standard conversion factors provided in the SAS watchout web page³. Hence, assuming $R_V=3.1$, we corrected all the fluxes for the Galactic reddening ($E_{B-V} = 0.39$, Schlafly & Finkbeiner 2011). For the correction, we used the IDL routine `ccm_unred`, which dereddens a user-defined vector of fluxes using the Galactic extinction curve of Cardelli et al. (1989).

3. Spectral energy distribution

As the preliminary step of our analysis we constructed the spectral energy distribution (SED) of the source. This is needed for the photoionization modeling of the absorbers.

The OM fluxes together with the EPIC-pn spectrum constrain the SED from optical/UV up to X-ray energies. We fitted the EPIC-pn data with a phenomenological model including a blackbody ($T_{\text{BB}} = 109$ keV) at soft energies, a power law ($\Gamma = 1.7$) at hard energies, and a broad Fe K α line ($FWHM=0.5$ keV). All these components are absorbed by the Galactic column density of $N_{\text{H}} = 2.31 \times 10^{21}$ cm⁻² (see the discussion below). We adopted the unabsorbed phenomenological continuum of this fit as the X-ray SED. Combining this X-ray continuum (Fig. 1, open squares) with the OM fluxes corrected for the Galactic extinction (Fig. 1, filled circles) we obtained the SED shown in Fig 1. We cut off the SED at low and high energy, respectively at 0.01 Ryd and 100 keV.

4. Spectral analysis

4.1. Galactic absorption

The X-ray spectrum of 4C +74.26 showed a heavy soft X-ray absorption in excess at the Galactic column measured by 21 cm surveys (e.g., $N_{\text{H}} = 1.16 \times 10^{21}$ cm⁻², Kalberla et al. 2005) in all the historical records (Sect. 1). We illustrate this by using our phenomenological fit of the EPIC-pn spectrum (Sect. 3). In Fig. 3, we show the confidence contour (i.e., curves of constant ΔC) of the N_{H} excess as a function of the modified blackbody normalization (left panel) and of power-law slope (right panel). An excess of N_{H} of at least $\sim 1.5 \times 10^{21}$ cm⁻² is observed in both figures at a confidence level of 99.99%.

Part of this excess of absorption can be due to the gas in our Galaxy rather than to some absorber intrinsic to the source. The total foreground X-ray absorption may be, in some cases, significantly larger than the value inferred using the N_{H} value provided by 21 cm surveys (Kalberla et al. 2005; Dickey & Lockman 1990). The difference may be ascribed to the presence of hydrogen in molecular form (H_2) in the Galactic ISM (Arabadjis & Bregman 1999), which is indeed elusive to 21 cm measurements. We used the calibration of Willingale et al. (2013)⁴ to infer the equivalent hydrogen column density of the the molecular hydrogen (N_{H_2}) along the line of sight of 4C +74.26. We found $N_{\text{H}_2} = 1.15 \times 10^{21}$ cm⁻². Thus, the total Galactic hydrogen column density absorbing the X-ray spectrum is $N_{\text{H}} + N_{\text{H}_2} = 2.31 \times 10^{21}$ cm⁻², consistent with the total column density inferred from the broadband X-ray spectrum (Ballantyne 2005). Applying the standard Galactic E_{B-V} / N_{H} ratio (1.77×10^{-22} , Predehl & Schmitt 1995), this hydrogen column density is also consistent with the Galactic reddening of $E_{B-V} = 0.39$ (Schlafly & Finkbeiner 2011). We use

¹ <http://tgcat.mit.edu/>

² <http://xmm.esac.esa.int/xsa/>

³ http://xmm.vilspa.esa.es/sas/7.1.0/watchout/Evergreen_tips_and_tricks/uvflux_old.shtml

⁴ <http://www.swift.ac.uk/analysis/nhtot/index.php>

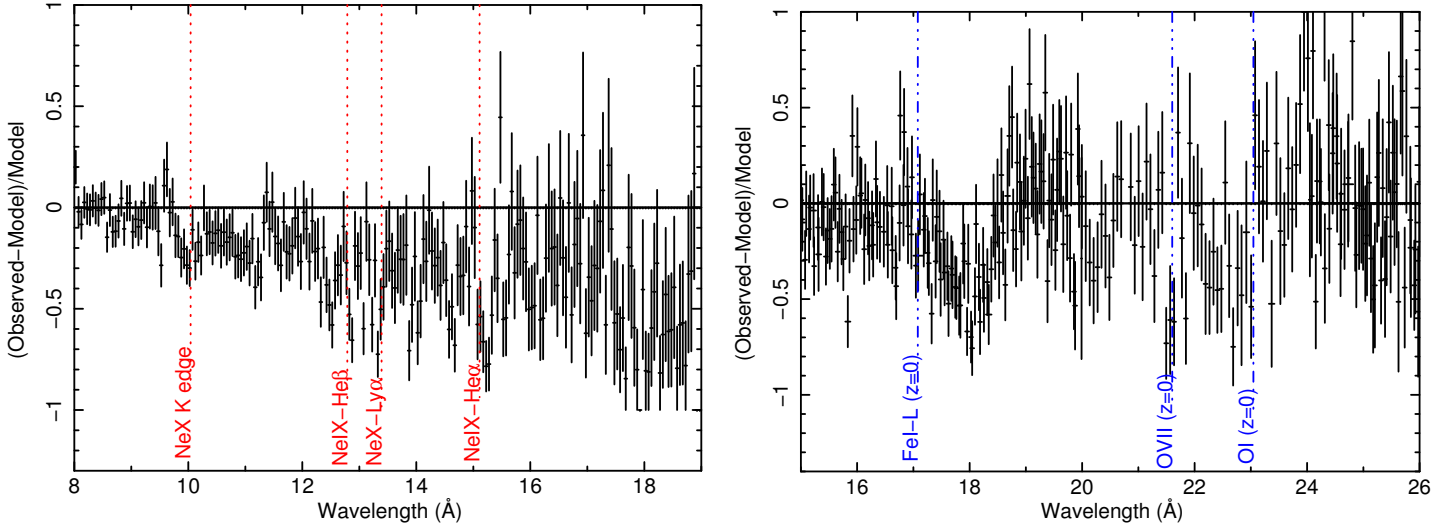


Fig. 2. Relative residuals of the MEG (*left panel*) and the RGS (*right panel*) spectrum after a simple power-law fit. Vertical lines indicate the wavelengths of the Galactic (triple-dot-dashed line) and intrinsic (dashed line) candidate absorption lines and edges. The spectra have been rebinned for clarity.

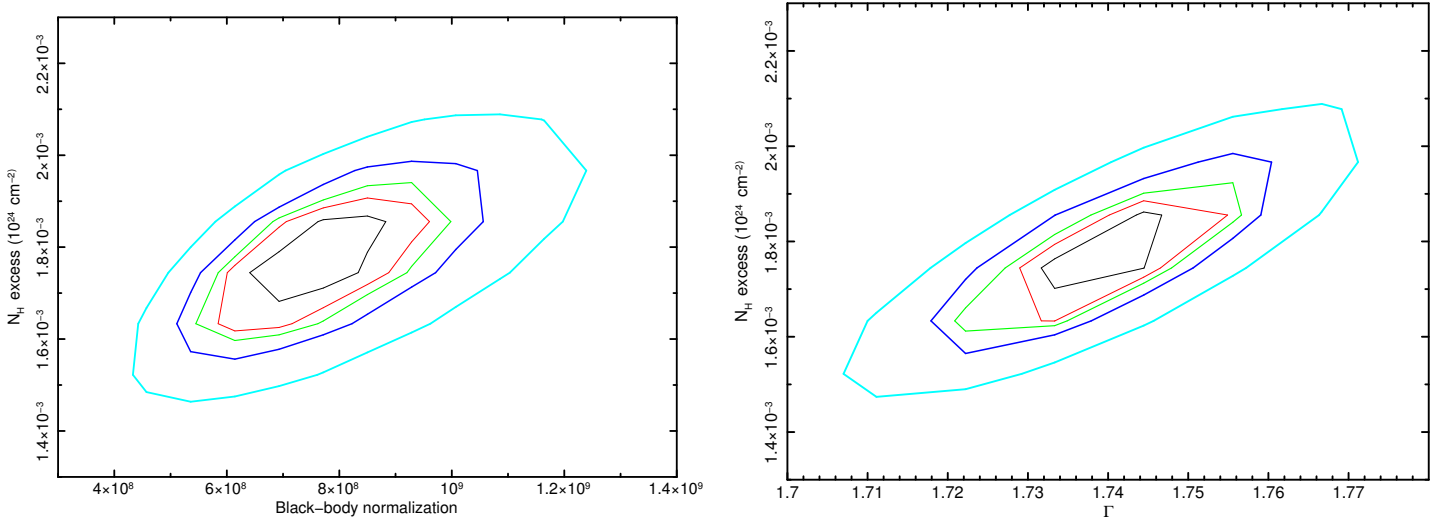


Fig. 3. Confidence level contour plot for the excess of N_{H} at the Galactic value of Kalberla et al. (2005) vs the normalization of the modified blackbody (*left panel*) and the power-law slope (*right panel*). The curves were obtained from a phenomenological fit of the EPIC-pn (Sect. 3). In each panel, the curves corresponding to a confidence level of 68%, 90%, 99%, and 99.99% are shown.

this Galactic column density value in all the spectral analyses performed here. The remainder of the excess absorption is due to the photoionized gas of the outflow (see Sect. 4.8). In fact, as our model shows, there is no need for additional neutral gas when this outflow is taken into account.

4.2. Preliminary spectral residuals

We performed the spectral analysis of the RGS and the HEG datasets using SPEX, version 3.0 (Kaastra et al. 1996). We began by fitting the RGS spectrum with a simple power-law continuum absorbed by the Galactic hydrogen column density and we inspected the relative residuals (Fig. 2, right panel). The most prominent features in the RGS residuals is a broad absorption trough visible at $\sim 18 \text{ \AA}$. We note that the Fe-L edges from the neutral absorber in our Galaxy cannot be responsible for this feature, as they would be expected at $\sim 17.1 \text{ \AA}$. Moving

redward, a narrow feature is clearly visible located at the wavelength expected for the O VII absorption line ($\sim 21.6 \text{ \AA}$) at redshift zero. Between 23 \AA and 24 \AA , where redshifted O VII transitions are expected, the residuals are systematically positive. This structure is a candidate broad emission line. Absorption from other transitions of ionized oxygen are also expected in this crowded spectral region (e.g., Detmers et al. 2011). We repeated this exercise for the HETGS spectrum. Guided by the knowledge of the RGS spectrum, we were able to recognize in the MEG the same absorption trough at $\sim 18 \text{ \AA}$. In the MEG this falls towards the end of the sensitive band, where the effective area starts degrading. Blueward of this, between 10 and 15 \AA , the HETGS residuals show some candidate absorption lines from the main Ne IX–Ne X transitions, indicating that some photoionized absorption may affect this spectrum.

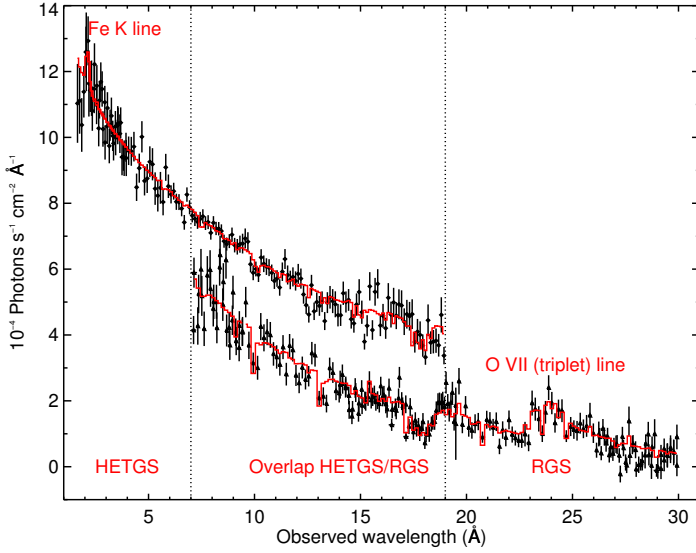


Fig. 4. Best fit of the RGS and of the HETGS spectrum of 4C +74.26. The diamonds and the triangles indicate the HETGS and the RGS data points, respectively. The HETGS spectrum has been shifted upwards ($\times 3$) for display purpose. Vertical lines indicate the band where the instruments overlap. The solid lines represent our best fit models. Emission lines are labeled. The spectra have been rebinned for clarity.

4.3. Setup of the joint RGS/HETGS fit.

The qualitative analysis of the RGS and MEG spectra shows hints of a complex ionized absorption in this source.

In order to accurately disentangle the multiple absorption components of this spectrum, we fit jointly the RGS and the HETGS datasets. The negligible variation in observed flux during the ~ 4 months separating these two observations (Table 1) is indeed an indication that the source and the absorbers were in the same conditions when these two spectra were taken. With a joint fit we take advantage of the high HETGS spectral resolution at short wavelengths, where most of the features from higher ionization species are expected, and of the high sensitivity of the RGS at long wavelengths, where the absorption features of e.g., ionized iron and oxygen reside.

In the fit, we used the RGS between 7 and 30 Å and the MEG between 2 and 19 Å. The quality of the HEG spectrum is worse than the MEG, thus we use HEG only in the Fe $K\alpha$ region between 1.5 and 5 Å. For the joint fit, we created two spectral sectors in SPEX, one for the RGS (RGS 1 and RGS 2) and one for the HETGS (HEG and MEG). In this way, each instrument is fitted independently, but the model parameters can be coupled. In the following, we fit jointly the HETGS and the RGS tying the absorption components together but allowing the continua to vary. In Fig. 4 we show the final best fit model in the total energy range covered.

4.4. Continuum

We set a simple continuum model comprising a power law and a phenomenological modified blackbody mimicking a soft-excess (Singh et al. 1985) component. For the latter we used the MBB model in SPEX, which includes the effect of Compton scattering (Kaastra & Barr 1989). In the fit we always kept the modified blackbody temperature of the HETGS model coupled to the RGS value because in our fit the band where the soft-excess component is supposed to dominate is mostly covered by the

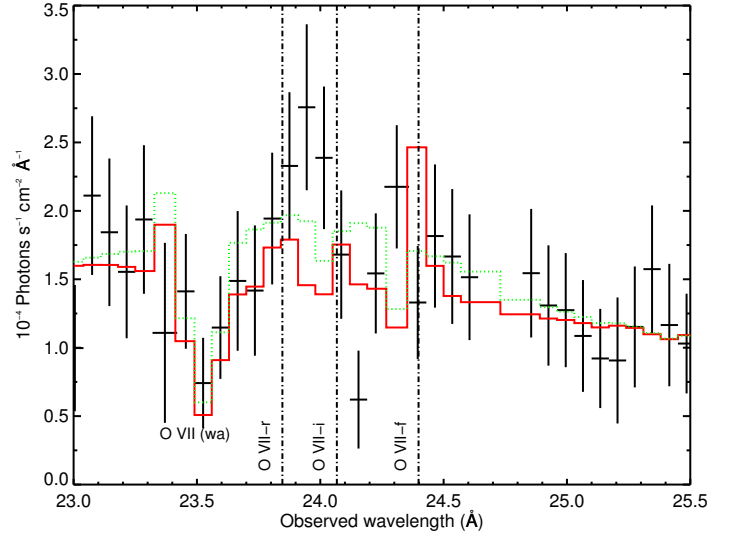


Fig. 5. RGS-1 spectrum of 4C +74.26 in the 23.0–25.5 wavelength region. The vertical dash-dotted lines mark the positions of the resonance, intercombination, and forbidden lines. The solid line represents the fit with a narrow profiled O VII triplet, which we were forced to reject (see Sect. 4.5). The dotted line represents our best fit model with a single Gaussian line representing a broadened O VII triplet. In both cases, the triplet profile is affected by absorption from ionized oxygen (O VII) intrinsic to the source as labeled. The spectrum has been rebinned for clarity.

RGS. For the power-law component, we set the initial value of the slope to that determined by the EPIC-pn fit. As the best fit was reached, the value of Γ settled at 1.67 ± 0.05 , while we found $T_{\text{BB}} = 170 \pm 15$ eV. The final best fit values for the continua are given in Table 2, first and second panel. A small difference in the normalizations of the continuum components is sufficient to account for the change of flux between the HETGS and the RGS observations.

4.5. Emission lines

The presence of a broad Fe $K\alpha$ emission line in 4C +74.26 is well established (Ballantyne & Fabian 2005; Larsson et al. 2008). The line is also clearly visible in the HETGS data (Fig. 4). We fitted it with a phenomenological Gaussian emission line with free centroid, width, and normalization. The values we obtained (Table 2, third panel) are consistent both with what is reported in the literature (Ballantyne 2005) and with our phenomenological fit of the EPIC-pn (Sect. 3).

In Fig. 5, we show the spectrum in the 23–25.5 Å range where we already noticed an excess in the residuals (Sect. 4.2) reminiscent of a broad emission line. At first, we tested whether these residuals could be accounted for with a narrow-profiled O VII triplet. We added to the fit three delta-profiled emission lines (DELTA model in SPEX) for the resonance ($\lambda=21.6$ Å), intercombination ($\lambda=21.8$ Å), and forbidden line ($\lambda=21.1$ Å). We left the normalization of the forbidden line free to vary and we assumed a ratio 1:3 for the other lines, as expected if photoionization occurs in a low-density plasma approximation (Porquet & Dubau 2000). This fit (Fig. 5) does not reproduce the data well and leaves large residuals between 23 and 24 Å.

Thus, we added to the fit a Gaussian profiled emission line. We left the line centroid free to vary among the nominal wavelengths of the O VII triplet and we used the width of the broad $H\alpha$ line given in Winter et al. (2010) to set the fitting range for the width

Table 2. Best fit parameters and errors for the final best fit model. Parameters without errors were kept coupled in the fit either to the RGS or to the HETGS value.

Model component	Parameter	RGS value	HETGS value	Units
Power law	Γ^a	1.67 ± 0.05	1.68 ± 0.02	
	$L_{0.3-10.0\text{keV}}^b$	13.7 ± 0.5	11.4 ± 0.3	$10^{44} \text{ erg s}^{-1}$
Blackbody	T_{BB}^c	170 ± 15	170	eV
	$L_{0.3-10.0\text{keV}}^b$	1.7 ± 0.8	1.0 ± 0.8	$10^{44} \text{ erg s}^{-1}$
Fe K α line	w^d	1.92	1.92 ± 0.08	\AA
	$FWHM^e$	0.16	0.16 ± 0.13	\AA
	$L_{\text{Fe K}\alpha \text{ line}}^b$	7	6 ± 4	$10^{42} \text{ erg s}^{-1}$
O VII (triplet) line	w^d	21.7 ± 0.1	21.7	\AA
	$FWHM^e$	1.0 ± 0.3	1.0	\AA
	$L_{\text{O VII line}}^b$	9 ± 3	9	$10^{42} \text{ erg s}^{-1}$
Warm Galactic absorber	N_{H}^f	2 ± 1	1.2	10^{20} cm^{-2}
	T^g	0.23 ± 0.04	0.20	keV
Intrinsic warm absorber	N_{H}^f	3.5 ± 0.6	3.1 ± 0.3	10^{21} cm^{-2}
	$\log \xi^h$	2.5 ± 0.1	2.57 ± 0.06	erg cm s^{-1}
	v_{out}^i	3600	3600 ± 70	km s^{-1}

Notes. ^(a) Power-law slope. ^(b) Model component luminosity, in the quoted band. ^(c) Blackbody temperature. ^(d) Wavelength of the line centroid. ^(e) Full width at half maximum of the line. ^(f) Absorber column density. ^(g) Absorber temperature. ^(h) Absorber ionization parameter. ⁽ⁱ⁾ Absorber outflow velocity.**Table 3.** Identification of the main absorption features in the RGS and in the HETGS spectrum of 4C +74.26.

Wavelength ^a	z^b	v_{out}^c	ΔC^d	Ion	Identification
\AA		km s^{-1}			Transition
21.602	0.104	2100 ± 900	-9	O VII	$1s^2 - 1s2p^1 P_1$
21.602	0	0	-14	O VII	$1s^2 - 1s2p^1 P_1$
13.447	0.104	3900 ± 200	-96	Ne IX	$1s^2 - 1s2p^1 P_1$
13.447	0	0	-47	Ne IX	$1s^2 - 1s2p^1 P_1$
12.132	0.104	4100 ± 300	-52	Ne X	$1s - 2p \text{ (Ly } \alpha)$
9.378 *	0.104			Mg IX	$2s^2 - 1s2s^2 2p$
9.281 *	0.104	3600 ± 100	-85	Mg X	$1s^2(^1S)2s - 1s(^2S)2s2p(^3P^0)$
9.169 *	0.104			Mg XI	$1s^2 - 1s2p^1 P_1$

Notes. ^(a) Nominal laboratory wavelength of the line. ^(b) Redshift applied. ^(c) Blueshift applied. ^(d) Improvement of the C-statistics with respect to a model including only the continuum, the emission lines, and the Galactic neutral absorber. ^(*) Lines fitted simultaneously with the same blueshift.

of a blended triplet ($FWHM=[0.36-1.23]\text{\AA}$). A broad O VII line having $FWHM=1.0 \pm 0.3$ better accounts for the excess in the residuals in the 23–25.5 \AA region. For the final fit, the statistical improvement produced by the addition of the O VII broad line is $\Delta C = -24$ for three additional degrees of freedom. An F-test gives a probability of a chance improvement of $\sim 10^{-5}$. In this fit the normalization of the narrow components goes to zero, indicating that the data quality does not allow them to be deblended from the broad component. The modeling of the broad emission line is critical for a correct evaluation of the absorption (e.g., Costantini et al. 2007; Di Gesu et al. 2013) because many transitions from ionized oxygen may in principle be detected within the line profile. We outline in Table 2, third and fourth panel, the final best fit values for the line parameters.

4.6. Line-by-line fitting of the absorption features

Before proceeding with a global modeling of the absorbing components, we first attempted to identify the absorption features of the spectrum on a line-by-line basis (e.g., Ebrero et al. 2013). We note, however, that not all the WA features can be identified with this method because of blending with neighboring transitions (e.g., the Fe-UTA) or with other components (e.g., Galactic). Moreover, only a global modeling is able to account

for the additional continuum curvature produced, for example, by an ionized absorber.

We visually identified in the spectrum the most prominent features, and for each of these we added to the model a Gaussian profiled absorption line multiplied by a blueshift model. The line centroid was set to the wavelength of the nearest known transition, while the line FWHM was set to the default value of 0.1 \AA . Thus, in this exercise, the free parameters were the line normalization and the blueshift.

In Table 3 we list our line identifications. In the RGS band we detected an O VII resonance line at redshift zero and at the redshift of 4C +74.26. The addition of an O VIII-Ly α line ($\lambda = 18.97 \text{\AA}$) line at the redshift of the source resulted instead in a negligible improvement of the fit ($\Delta C=-3$). In the HETGS band, we detected absorption from Ne IX at redshift 0 and from Ne IX, Ne X, Mg IX, Mg X, and Mg XI in the source rest-frame. The magnesium lines are blended, so we fitted them simultaneously with the same blueshift. All the lines detected in the HETGS band show a similar blueshift, suggesting that they may be part of the same outflowing system.

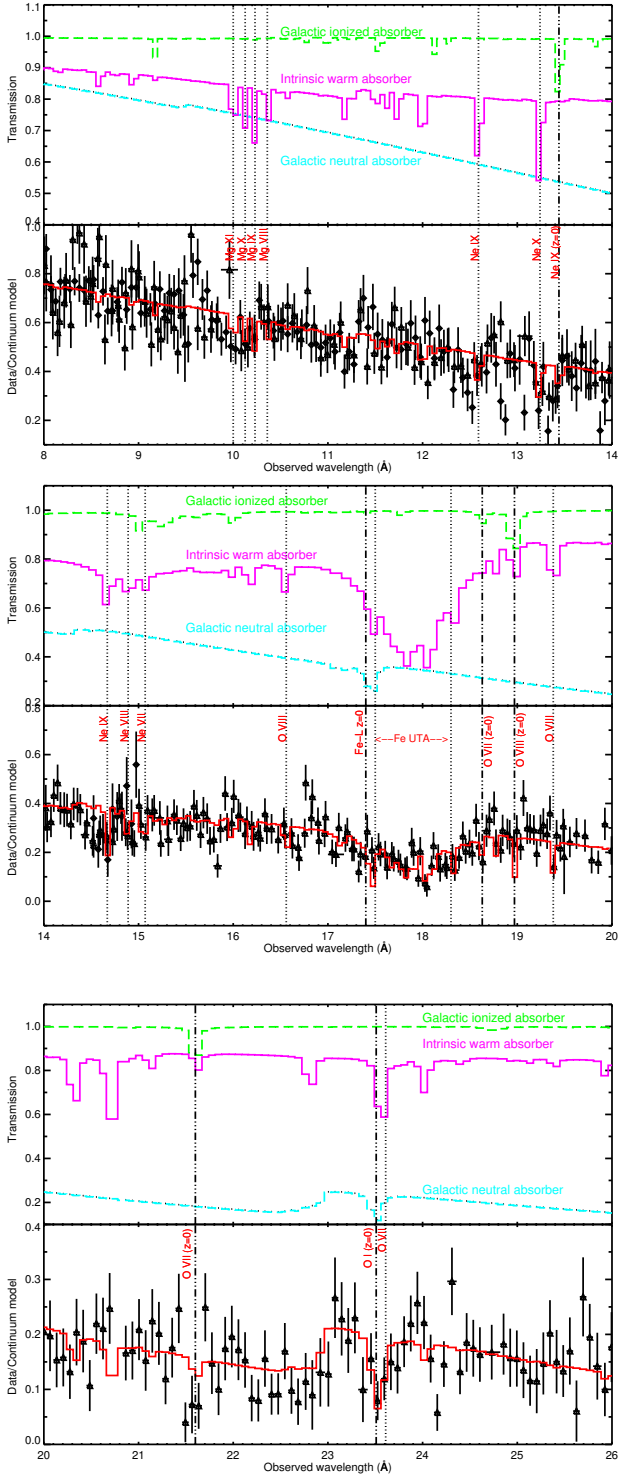


Fig. 6. From top to bottom: Absorption features of 4C +74.26 in the 8–14 Å (*upper figure*), 14–20 Å (*middle figure*), and 20–26 Å band (*lower figure*). In each figure the transmission (*upper panel*) of the Galactic (long-dashed lines) and intrinsic (solid line) absorbing components is shown together with the ratio between the data and the continuum model (*lower panel*), highlighting the absorption features. The HETGS and the RGS data points are plotted as diamonds and triangles, respectively. The solid line represent the best fit model. Vertical lines mark the position of the most prominent Galactic (double-dot-dashed lines) and intrinsic (dotted lines) absorption features.

4.7. Absorption at redshift zero

We modeled the Galactic cold absorption using a collisionally ionized plasma model in SPEX (HOT), setting a temperature of 0.5 eV for the neutral gas case. This component produces O I and Fe I absorption at ~ 23.5 Å and ~ 17.4 Å, respectively. As pointed out in Sect. 4.2 narrow absorption lines from O VII and Ne IX at redshift zero are detected respectively in the RGS and in the HETGS spectrum. These could originate in the warm plasma of the Galactic corona, which is collisionally ionized (e.g., Yao & Wang 2005; Pinto et al. 2012). To model it, we added another HOT component to the fit. We left both T and the gas column density N_{H} free to vary. We kept instead the broadening velocity frozen to the default value of 100 km s^{-1} . The final best fit values that we found for all these free parameters are listed in Table 2, fifth panel.

4.8. Intrinsic photoionized absorption

We modeled the intrinsic photoionized absorption using the XABS model in SPEX which computes the transmission of a slab of material where all the ionic column densities are linked to each other through the photoionization balance prescribed by the SED (Fig. 1). We computed the SED with the SPEX auxiliary tool XABSINPUT and the photoionization code Cloudy (Ferland et al. 2013), version 13.01. For the XABS component, we allowed the column density, the ionization parameter, and the outflow velocity of the gas to vary, while we kept the broadening velocity frozen to the default value of 100 km s^{-1} .

We found that an intrinsic photoionized absorber with $N_{\text{H}} \sim 3 \times 10^{21} \text{ cm}^{-2}$ and $\log \xi \sim 2.6$ best fits the candidate absorption features of the spectrum. The systematic blueshift of the lines corresponds to an outflow velocity of $v_{\text{out}} \sim 3600 \text{ km s}^{-1}$. We list in Table 2, sixth panel, the best fit parameters for the WA. After achieving the best fit, we decoupled the column density and the ionization parameter of the RGS model from the HETGS values to check for a possible time variability of the WA in the 4 months separating the HETGS from the RGS observation. We found that during this time interval the WA parameters are consistent not to have varied. We note that a one-zone WA is sufficient to best fit the ionized absorption features of the spectrum. Indeed, the fit erases any additional ionized absorbing components, either photoionized or collisionally ionized. The final C-statistics for a model including two Galactic absorbers and an intrinsic WA is $C/\text{Expected } C = 1065/931$.

In Fig. 6, we show the transmission of all the absorbing components of the model, together with the ratio between the data and the continuum model, which highlights the absorption features. In the RGS band the most evident WA feature is the broad absorption trough visible at ~ 18 Å. This is mostly produced by the unresolved transitions array (UTA) from the ionized iron (e.g., Fe x–Fe xx) contained in the photoionized gas. In addition, a O VII absorption line is prominent at ~ 23.5 Å. This feature is blended with the O I line from the neutral absorber in the Galaxy. In the HETGS band, the absorption lines are weak. The most apparent features are from highly ionized species, such as Ne VII–Ne x and Mg VIII–Mg xi.

5. Discussion

We have presented a joint analysis of the RGS and HETGS spectra of the heavily X-ray absorbed radio-loud quasar 4C +74.26. Thanks to the high spectral resolution of these grating spectra, we were able to reveal a rich spectrum of absorption fea-

tures originating from both Galactic and intrinsic material. In our analysis we used the total Galactic column density given in Willingale et al. (2013), which includes the contribution of molecular hydrogen. This is roughly twice the value provided by 21 cm surveys. The enhanced Galactic absorption explains the heavy suppression of the soft X-ray flux that was noticed in the past for this source (Brinkmann et al. 1998; Sambruna et al. 1999; Reeves & Turner 2000; Hasenkopf et al. 2002; Ballantyne & Fabian 2005).

The intrinsic absorption comprises a highly ionized WA which produces a deep Fe-UTA trough in the RGS and the weak absorption features that are visible in the HETGS spectrum. We found that an outflow velocity of $\sim 3600 \text{ km s}^{-1}$ is required for a best fit of the absorption features visible in the two spectra. This finding is evidence for WA absorption in radio-loud objects, which so far has been scarce. Indeed, in addition to 3C 382, 3C 445 and 3C 390.3, 4C +74.26 is the fourth radio-loud source where a photoionized outflow has been clearly characterized in a high-resolution dataset. The column density, ionization parameter, and outflow velocity that we measured for the WA in 4C +74.26 are within the range observed in Seyfert 1 galaxies (McKernan et al. 2007) and are also in line with the values found in 3C 382 and 3C 390.3, the other two radio-loud galaxies hosting a classical WA. The case of 3C 445 is an outlier, as this source hosts a high-velocity, high-column UFO-like wind (see the review of Torresi et al. 2012).

In the following sections we use the results of our spectral analysis and the information from the literature to infer a possible geometrical model for the outflow in this AGN. To this purpose, in Sect. 5.1 we estimate the possible location and the energetics of the warm absorber. In Table 4, upper panel, we outline some basic physical properties of the source that serve for an order of magnitude comparison. We took the black hole mass M_{BH} and the source inclination i from the literature as already explained in Sect. 1. From a numerical integration of the SED of Fig. 1 we computed the ionizing luminosity L_{ION} between 1 and 1000 Ry and the bolometric luminosity over the whole optical and X-ray band. We note that the bolometric luminosity is probably underestimated because the radio emission at low energies and the gamma ray emission at high energies are not included in our SED. Hence, using these data we estimated the Eddington luminosity L_{Edd} and the mass accretion rate \dot{M}_{acc} , for which we assumed an accretion efficiency $\eta = 0.1$. For the jet power P_{jet} we used the radio flux at 1.4 GHz (Condon et al. 1998) and the scaling relationship of Cavagnolo et al. (2010). The radius of the broad line region R_{BLR} scales with the optical luminosity at 5100 Å (Wandel 2002). The luminosity value is given in Winter et al. (2010). Finally, the radius of the putative torus R_{TOR} , which is nominally set by the dust sublimation radius, scales with L_{ion} (Krolik & Kriss 2001).

5.1. Location and energetics of the ionized outflow

In Table 4, lower panel, we outline some physical properties of the ionized outflow that we estimated using our measured parameters, namely $N_{\text{H}} \sim 3.1 \times 10^{21} \text{ cm}^{-2}$, $\log \xi \sim 2.6$, and $v_{\text{out}} \sim 3600 \text{ km s}^{-1}$. We follow here the argumentation of Blustein et al. (2005), which assumes that the outflow is a partially filled spherical shell of gas with a volume filling factor f . An analytical expression for the volume filling factor f is derived in Blustein et al. (2005) from the prescription that the kinetic momentum of the outflow must be on the order of the momentum of the absorbed radiation plus the momentum of the scattered radiation.

For the ionized outflow in 4C +74.26 we found that the ionized gas fills only $\sim 0.007\%$ of the spherical volume, which suggests that it may consist of sparse clumps.

We set a range of possible distances for the absorber from the conditions that the velocity of the outflow must exceed the escape velocity from the AGN and that the outflowing shell must not be thicker than its distance from the center ($\Delta r/R \leq 1$). Analytically,

$$\frac{2GM_{\text{BH}}}{v^2} \leq R \leq \frac{L_{\text{ion}}f}{\xi N_{\text{H}}},$$

where G is the gravitational constant. For our parameters, both these expressions return a value of $\sim 2 \text{ pc}$ (Table 4). This constrains the ionized outflow of 4C +74.26 to be located outside the BLR ($R_{\text{BLR}} = 0.2 \text{ pc}$), but within the boundary of the putative torus ($R_{\text{TOR}} = 6 \text{ pc}$).

A patchy ionized outflow located outside the BLR is a natural candidate for being the scattering outflow that is required in the Robinson et al. (1999) analysis of the polarized optical spectrum of this source. Their model prescribes that the observed redshift of the polarized H α line is due to a high-velocity motion of the scattering material which polarizes the BLR light. In this framework, the outflow velocity inferred for the scatterer depends on the inclination of the scattering cone with respect to the jet axis. For the case of a scattering outflow coaligned with the radio jet, they quote a velocity of $\sim 5000 \text{ km s}^{-1}$. Interestingly, if we consider the same source inclination used in the Robinson et al. (1999) model ($\sim 45^\circ$) and we assume that the WA found in our analysis is outflowing along the polar axis of the source, we obtain a deprojected velocity of $v_{\text{out}}/\cos 45^\circ \sim 5000 \text{ km s}^{-1}$ (Fig. 7). This matches the Robinson et al. (1999) prediction. This correspondence hints at the possibility that the WA detected here and the outflowing polar scatterer discovered in Robinson et al. (1999) are one and the same.

Given the velocity, the mass outflow rate is given by

$$\dot{M}_{\text{out}} = \frac{1.23m_p L_{\text{ion}}f v_{\text{out}} \Omega}{\xi},$$

where m_p is the proton mass and Ω is the solid angle of the outflow, which we set to 2.1 sr, as in Torresi et al. (2012). This is derived assuming that at least 50% of radio-loud objects host an outflow, like in a Seyfert galaxy, and using the information that $\sim 33\%$ of the radio galaxies belonging to the 3CR sample are type 1 AGN (Buttiglione et al. 2009). Hence, using the mass outflow rate, the kinetic luminosity of the outflow is readily computed as $L_{\text{kin}} = \frac{1}{2} \dot{M}_{\text{out}} v_{\text{out}}^2$.

The value we obtained for the kinetic luminosity is at least four orders of magnitude lower than the bolometric luminosity. Theoretical AGN feedback models (e.g., Di Matteo et al. 2005; Hopkins & Elvis 2010) typically require kinetic luminosities comparable with the bolometric luminosity for an outflow to be able to halt the star formation in a typical galactic bulge. Thus, this outflow is unable to deliver a significant feedback in this AGN. Moreover, as found for the other radio-loud galaxies hosting a WA, the kinetic luminosity of the outflow is negligible compared to the jet power ($L_{\text{kin}} \sim 10^{-2} P_{\text{jet}}$). Thus, the case of 4C +74.26 confirms that the jet is a more likely driver of AGN feedback in radio-loud galaxies (Torresi et al. 2012).

6. Summary

We performed a joint analysis of the RGS and HETGS spectra of the radio-loud quasar 4C +74.26. The spectrum is affected

Table 4. Properties of 4C +74.26.

Source properties	Ref
$M_{\text{BH}} = 3 \times 10^9 M_{\odot}$	Winter et al. (2010)
$i \leq 49^{\circ}$	Pearson et al. (1992)
$L_{\text{bol}} = 9.7 \times 10^{46} \text{ erg s}^{-1}$	Sect. 5
$L_{\text{bol}}/L_{\text{Edd}} = 0.25$	Sect. 5
$\dot{M}_{\text{acc}} = 17 M_{\odot} \text{ yr}^{-1}$	Sect. 5
$L_{\text{ion}} = 8.8 \times 10^{46} \text{ erg s}^{-1}$	Sect. 5
$P_{\text{jet}} = 2 \times 10^{44} \text{ erg s}^{-1}$	Sect. 5
$P_{\text{jet}}/L_{\text{Edd}} = 6 \times 10^{-4}$	Sect. 5
$R_{\text{BLR}} = 0.2 \text{ pc}$	Sect. 5
$R_{\text{TOR}} = 6 \text{ pc}$	Sect. 5
Ionized outflow properties	Ref
$1.6 \leq R \leq 1.8 \text{ pc}$	Sect. 5.1
$f = 7 \times 10^{-5}$	Sect. 5.1
$\dot{M}_{\text{out}} = 0.4 M_{\odot} \text{ yr}^{-1}$	Sect. 5.1
$L_{\text{kin}} = 1.5 \times 10^{42}$	Sect. 5.1

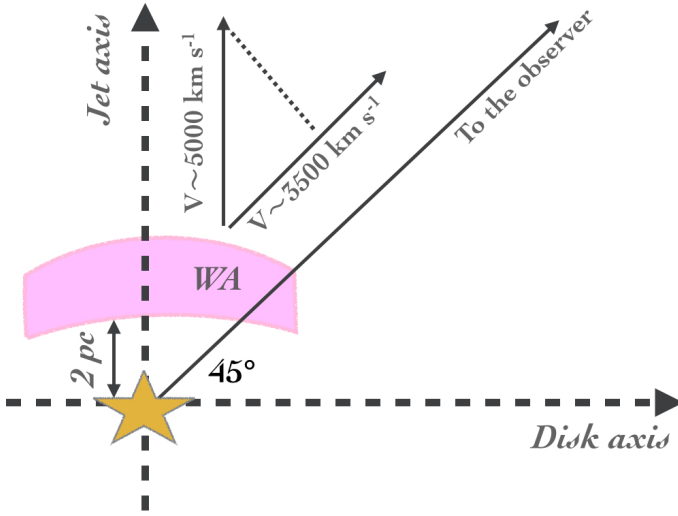


Fig. 7. Outflow in the inner region of 4C +74.26. The observer's line of sight lies at 45° from the jet axis. The WA is part of a polar outflow located outside the BLR. The ionized gas outflows along the polar direction with a velocity of $\sim 5000 \text{ km s}^{-1}$, which is observed as $\sim 3500 \text{ km s}^{-1}$ from the observer's inclination angle.

by a heavy X-ray absorption arising from both Galactic and intrinsic material.

Most of the absorption in the soft X-ray band is due to the Galactic ISM. We point out that when also considering the contribution of molecular hydrogen, the total Galactic N_{H} is roughly twice the standard value provided by 21 cm surveys.

A photoionized outflow ($N_{\text{H}} \sim 3.2 \sim 10^{21} \text{ cm}^{-2}$, $\log \xi \sim 2.6$, $v_{\text{out}} \sim 3600 \text{ km s}^{-1}$) located at the source rest-frame produces a sharp Fe-UTA trough in the RGS and the weak absorption features visible in the HETGS. The kinetic luminosity carried by the outflowing gas ($L_{\text{kin}} \sim 10^{-5} L_{\text{bol}}$) is negligible for the AGN feedback in this source.

We discuss a scenario where the photoionized gas is part of a polar-scattering outflow, also detected in the optical-polarized spectrum.

Acknowledgements. The scientific results are based on data obtained from the Chandra and the XMM-Newton data archives. SRON is supported financially by NWO, the Netherlands Organization for Scientific Research. LDG acknowl-

edges support from the Swiss National Science Foundation. We thank Enrico Piconcelli, Margherita Giustini, and Francesco Tombesi for useful discussions. We thank Jelle Kaastra and Missagh Mehdipour for commenting and carefully reading this manuscript.

References

- Arabadjis, J. S. & Bregman, J. N. 1999, *ApJ*, 510, 806
Ballantyne, D. R. 2005, *MNRAS*, 362, 1183
Ballantyne, D. R. & Fabian, A. C. 2005, *ApJ*, 622, L97
Blustin, A. J., Page, M. J., Fuerst, S. V., Branduardi-Raymont, G., & Ashton, C. E. 2005, *A&A*, 431, 111
Boissay, R., Ricci, C., & Paltani, S. 2016, *A&A*, 588, A70
Braito, V., Reeves, J. N., Sambruna, R. M., & Gofford, J. 2011, *MNRAS*, 414, 2739
Brinkmann, W., Otani, C., Wagner, S. J., & Siebert, J. 1998, *A&A*, 330, 67
Buttiglione, S., Capetti, A., Celotti, A., et al. 2009, *A&A*, 495, 1033
Cardelli, J. A., Clayton, G. C., & Mathis, J. S. 1989, *ApJ*, 345, 245
Cash, W. 1979, *ApJ*, 228, 939
Cavagnolo, K. W., McNamara, B. R., Nulsen, P. E. J., et al. 2010, *ApJ*, 720, 1066
Condon, J. J., Cotton, W. D., Greisen, E. W., et al. 1998, *AJ*, 115, 1693
Costantini, E. 2010, *Space Sci. Rev.*, 157, 265
Costantini, E., Kaastra, J. S., Arav, N., et al. 2007, *A&A*, 461, 121
Crenshaw, D. M. & Kraemer, S. B. 2012, *ApJ*, 753, 75
Crenshaw, D. M., Kraemer, S. B., & George, I. M. 2003, *ARA&A*, 41, 117
Detmers, R. G., Kaastra, J. S., Steenbrugge, K. C., et al. 2011, *A&A*, 534, A38
Di Gesu, L., Costantini, E., Arav, N., et al. 2013, *A&A*, 556, A94 (Paper I)
Di Gesu, L., Costantini, E., Piconcelli, E., et al. 2014, *A&A*, 563, A95
Di Matteo, T., Springel, V., & Hernquist, L. 2005, *Nature*, 433, 604
Dickey, J. M. & Lockman, F. J. 1990, *ARA&A*, 28, 215
Done, C., Davis, S. W., Jin, C., Blaes, O., & Ward, M. 2012, *MNRAS*, 420, 1848
Ebrero, J., Kaastra, J. S., Kriss, G. A., de Vries, C. P., & Costantini, E. 2013, *MNRAS*, 435, 3028
Ebrero, J., Kaastra, J. S., Kriss, G. A., et al. 2016, *A&A*, 587, A129
Ferland, G. J., Porter, R. L., van Hoof, P. A. M., et al. 2013, *Rev. Mexicana Astron. Astrofis.*, 49, 137
Fiore, F., Elvis, M., Mathur, S., Wilkes, B. J., & McDowell, J. C. 1993, *ApJ*, 415, 129
Giustini, M., Turner, T. J., Reeves, J. N., et al. 2015, *A&A*, 577, A8
Gofford, J., Reeves, J. N., Tombesi, F., et al. 2013, *MNRAS*, 430, 60
Hasenkopf, C. A., Sambruna, R. M., & Eracleous, M. 2002, *ApJ*, 575, 127
Hopkins, P. F. & Elvis, M. 2010, *MNRAS*, 401, 7
Hopkins, P. F., Hernquist, L., Cox, T. J., & Kereš, D. 2008, *ApJS*, 175, 356
Jin, C., Ward, M., Done, C., & Gelbord, J. 2012, *MNRAS*, 420, 1825
Kaastra, J. S. & Barr, P. 1989, *A&A*, 226, 59
Kaastra, J. S., Mewe, R., & Nieuwenhuijzen, H. 1996, in *UV and X-ray Spectroscopy of Astrophysical and Laboratory Plasmas*, ed. K. Yamashita & T. Watanabe, 411–414
Kalberla, P. M. W., Burton, W. B., Hartmann, D., et al. 2005, *A&A*, 440, 775
King, A. & Pounds, K. 2015, *ARA&A*, 53, 115
Krolik, J. H. & Kriss, G. A. 2001, *ApJ*, 561, 684
Larsson, J., Fabian, A. C., Ballantyne, D. R., & Miniutti, G. 2008, *MNRAS*, 388, 1037
Mathur, S. 1994, *ApJ*, 431, L75
Mathur, S., Wilkes, B., Elvis, M., & Fiore, F. 1994, *ApJ*, 434, 493
McKernan, B., Yaqoob, T., & Reynolds, C. S. 2007, *MNRAS*, 379, 1359
Molina, M., Venturi, T., Malizia, A., et al. 2015, *MNRAS*, 451, 2370
Nardini, E., Reeves, J. N., Gofford, J., et al. 2015, *Science*, 347, 860
Noda, H., Makishima, K., Nakazawa, K., et al. 2013, *PASJ*, 65
Noda, H., Makishima, K., Yamada, S., et al. 2011, *PASJ*, 63, S925
Pearson, T. J., Blundell, K. M., Riley, J. M., & Warner, P. J. 1992, *MNRAS*, 259, 13P
Petrucci, P.-O., Paltani, S., Malzac, J., et al. 2013, *A&A*, 549, A73
Pinto, C., Kriss, G. A., Kaastra, J. S., et al. 2012, *A&A*, 541, A147
Porquet, D. & Dubau, J. 2000, *A&AS*, 143, 495
Predehl, P. & Schmitt, J. H. M. M. 1995, *A&A*, 293, 889
Reeves, J. N., Gofford, J., Braito, V., & Sambruna, R. 2010, *ApJ*, 725, 803
Reeves, J. N., Sambruna, R. M., Braito, V., & Eracleous, M. 2009, *ApJ*, 702, L187
Reeves, J. N. & Turner, M. J. L. 2000, *MNRAS*, 316, 234
Riley, J. M. & Warner, P. J. 1990, *MNRAS*, 246, 1P
Riley, J. M., Warner, P. J., Rawlings, S., et al. 1989, *MNRAS*, 236, 13P
Robinson, A., Corbett, E. A., Axon, D. J., & Young, S. 1999, *MNRAS*, 305, 97
Sambruna, R. M., Eracleous, M., & Mushotzky, R. F. 1999, *ApJ*, 526, 60
Scannapieco, E. & Oh, S. P. 2004, *ApJ*, 608, 62
Schlafly, E. F. & Finkbeiner, D. P. 2011, *ApJ*, 737, 103
Singh, K. P., Garmire, G. P., & Nousek, J. 1985, *ApJ*, 297, 633

- Somerville, R. S., Hopkins, P. F., Cox, T. J., Robertson, B. E., & Hernquist, L. 2008, *MNRAS*, 391, 481
- Tombesi, F., Cappi, M., Reeves, J. N., & Braito, V. 2012, *MNRAS*, 422, 1
- Tombesi, F., Cappi, M., Reeves, J. N., et al. 2011, *ApJ*, 742, 44
- Tombesi, F., Cappi, M., Reeves, J. N., et al. 2010, *A&A*, 521, A57
- Tombesi, F., Tazaki, F., Mushotzky, R. F., et al. 2014, *MNRAS*, 443, 2154
- Torresi, E., Grandi, P., Costantini, E., & Palumbo, G. G. C. 2012, *MNRAS*, 419, 321
- Torresi, E., Grandi, P., Longinotti, A. L., et al. 2010, *MNRAS*, 401, L10
- Wandel, A. 2002, *ApJ*, 565, 762
- Willingale, R., Starling, R. L. C., Beardmore, A. P., Tanvir, N. R., & O'Brien, P. T. 2013, *MNRAS*, 431, 394
- Winter, L. M., Lewis, K. T., Koss, M., et al. 2010, *ApJ*, 710, 503
- Yao, Y. & Wang, Q. D. 2005, *ApJ*, 624, 751
- Yuan, Q., Green, R. F., Brotherton, M., et al. 2002, *ApJ*, 575, 687